A practical guide for setting up a Fourier lightfield microscope

H. YUN,[1] G. SAAVEDRA,[1] J. GARCIA-SUCERQUIA,[1,2] A. TOLOSA,[1] M. MARTINEZ-CORRAL,[1,*] AND E. SANCHEZ-ORTIGA[1,3]

[1]*3D Imaging and Display Laboratory. Department of Optics. University of Valencia. E46100, Burjassot, Spain*
[2]*Universidad Nacional de Colombia Sede Medellín, School of Physics, A.A: 3840-Medellín-050034, Colombia*
[3]*School of Science, Universidad Europea de Valencia, 46010 Valencia, Spain*
[*]*manuel.martinez@uv.es*

Abstract: A practical guide for the easy implementation of a Fourier Lightfield Microscope is reported. The Fourier Lightfield concept applied to microscopy allows the capture in real time of a series of 2D orthographic images of microscopic thick dynamic samples. Such perspective images contain the spatial and the angular information of the lightfield emitted by the sample. A feature of this technology is the tight requirement of a double optical conjugation relationship, and also the requirement of NA matching. For these reasons, being the Fourier Lightfield Microscope a non-complex optical system, a clear protocol on how to set up accurately the optical elements is needed. In this sense, this guide is aimed to simplify the implementation process, which will help the widespread of this recent technology. © 2022 Optica Publishing Group.

1. Introduction

Optical microscopes are designed for obtaining 2D images of small samples. Although it is commonly believed that the main feature of microscopes is their ability for providing highly magnified images, this is not entirely correct. This statement is more evident in the context of digital images, which can be easily magnified by a simple resizing operation, often performed with two fingers. Thus, high magnification is not a distinct feature, mainly in the digital world. Clearly, the main feature of microscopes is their capacity for producing images with high lateral resolution. Resolution is defined as the capability of an optical system for producing images in which the small details are distinguishable. Resolution is usually evaluated in terms of the Rayleigh criterion, which measures the minimum distance reachable between two equal-intensity point sources so that their images are still distinguishable. An alternative approach, due to Ernst Abbe, is to measure the cut-off spatial frequency. In any case, the two approaches provide similar results, which mainly depend on the numerical aperture (NA) of the microscope objective. Additionally, the influence of the pixel size must be taken also into account, especially when the pixel size is comparable with the Rayleigh resolution limit.

An important drawback of conventional microscopes is their performance when imaging 3D objects. In that case, the sensor captures a 2D image that is the result of collapsing onto the image plane the 3D image of the 3D sample. This includes the blurring associated with object planes out from the system's Depth of Field (DoF). As a result, the angular (or perspective) information of the sample is lost, even in the case that one captures a focal stack and builds a 3D image from it [1].

Aiming to overcome these problems, Lightfield Microscopy (LMic) was reported a few years ago [2–7]. LMic is based on the smart idea, reported by Lippmann [8], that a collection of perspective images of a 3D scene, stores both the spatial and the angular information of the rays emitted by the scene. Specifically, an LMic is built by inserting a microlens array (MLA)

at the image plane of a conventional microscope and shifting the sensor up to the microlenses rear focal plane. This capability of capturing in a single shot the spatial-angular information of 3D specimen, allows LMic to be specially adapted to deal with the 3D behavior of dynamic biological processes [6, 9–12].

However, the images captured with LMic still show the following drawbacks. (a) The perspective images (also known as elemental images – EI) are not obtained directly but computed from the captured microimages. (b) The lateral resolution of EIs is determined by the microlenses pitch, whereas the number of pixels covered by any microlens determines the density of the angular sampling. As consequence, LMic provides images with a spatial resolution that is about 10 times worse than that of the host microscope where the MLA is inserted. (c) The lateral resolution of computed depth sections is inhomogeneous. (d) The system is not linear and shift-invariant, and therefore not easy application of deconvolution tools is possible.

Naturally, much work has been reported aiming to overcome these drawbacks by computational means. However, such methods have to tackle two essential difficulties. One is that the images captured by LMic have a low spatial resolution, and therefore much high-frequency information has escaped, which cannot be recovered by digital processing. The other is the complexity of the deconvolution procedures application. This implies that the algorithms need to be highly sophisticated and time-consuming. Nevertheless, the results obtained by such computational methods are inspiring [13, 14].

To avoid these problems, Fourier Lightfield Microscopy (FLMic) was proposed [15–19]. FLMic is based on a new paradigm since the microlenses, whose pitch is now one order the magnitude bigger than in LMic, are placed no longer at the image plane but at its far field; the Fourier plane. Then the EIs are captured directly and have a spatial resolution that is 3 to 5 times worse than that of the host microscope, but 2 to 3 times better than in LMic. Importantly, here the captured EIs have shift invariance, which allows the direct use of deconvolution tools and the computing of depth sections that have homogeneous resolution through the system DoF. Another advantage of FLMic is that it can be implemented easily by inserting an accessory at the camera port of a conventional microscope, and therefore can make use of the usual facilities of such microscope as for example the dark-field illumination mode [20, 21].

Even though the impact aroused in the microscopy community [22–32], the generalization of the use of FLMic is still limited. One of the problems is the selection of the set of optical components, which must to fulfill many crossed relations. This problem was already addressed in our previous paper [33]. As a follow on to that paper, we still consider that it can be very useful to provide a similar tutorial on construction, alignment, and test/validation methods. This conviction has aimed this laboratory note, in which we show, step by step, a comprehensive guide for the accurate implementation of a FLMic.

2. Basic theory

Fourier lightfield microscopy (FLMic) is an optical technique that permits the direct capture of a series of orthographic perspective views of thick microscopic samples. The concept behind FLMic is simple; a microlens array (MLA) is inserted at the aperture stop (AS) of an infinity-corrected microscope objective (MO) and the sensor is set at the lenslets rear FP. This permits the simultaneous capture of orthographic images of the specimen. However, this preliminary scheme lacks flexibility, since the MLA must be fully adapted to the selected MO and also to the requirements in resolution and parallax. Then, if a researcher wanted to implement a FLMic in the laboratory, and aimed to have enough flexibility, it is preferable not to insert the MLA directly at the AS, but at a conjugate plane. This is achieved by using a telecentric relay ($L_{R1} + L_{R2}$) formed by two converging lenses and a circular aperture as shown in Fig. 1(a). Note that, since a FLMic deals with 3D samples, we must define a reference object plane (ROP) within the region of interest, which must be placed at the MO focal plane. As stated above, the

Table 1. List of acronyms used in the paper.

Acronym	Full name
AS	Aperture Stop
DoF	Depth of Field
EI	Elemental Image
FLMic	Fourier Lightfield Microscope
FOV	Field of View
FP	Focal Plane
FS	Field Stop
LED	Light Emitting Diode
LMic	Lightfield Microscope
MLA	Microlens Array
MO	Microscope Objective
NA	Numerical Aperture
ROP	Reference Object Plane
S & M	Shift and Multiply
S & S	Shift and Sum

conjugations relations are key. In this sense, the MO together with the first lens of the telecentric relay (L_{R1}) conform a telecentric coupling that conjugates the ROP with the back focal plane (FP) of L_{R1}, where a field stop (FS) is placed. Also, the image of the AS through L_{R1} is at the infinity. On the other hand, the telecentric relay provides the image of the AS at the rear focal plane of second lens of the telecentric relay (L_{R2}), where the MLA is placed. The image of the ROP is now at infinity. Finally, the microlenses provide multiple images (named as elemental images –EI) of the object at the lenslets rear focal plane, where the sensor is set.

In Fig. 1(b) we have made explicit the conjugation relation between the AS and the MLA by painting a shaded MLA at the AS. Also, we have represented with different colours the light beams that pass through different microlenses. Clearly, each microlens collects the light passing through a different, non-overlapping, region of the AS. The size of the AS determines the number of microlenses that fit into it, and then the number (N_{EI}) of captured EIs,

$$\mathrm{N}_{EI} = \frac{\phi_{AS}}{\hat{p}} = \frac{2 f_{ob} f_{R2} \mathrm{NA}}{f_{R1} p}, \tag{1}$$

where $\hat{p} = p f_{R1}/f_{R2}$ is the lenslets pitch, p, as back-projected onto the AS.

Conversely, the lenslets diameter determines the effective numerical aperture (NA) under which the EIs are captured. We can conclude from Fig. 1(a) that the FLMic captures N_{EI} images (along one Cartesian direction), each with different perspective information and under an effective NA given by

$$\mathrm{NA}_{\mathrm{ef}} = \frac{\mathrm{NA}}{N_{EI}}, \tag{2}$$

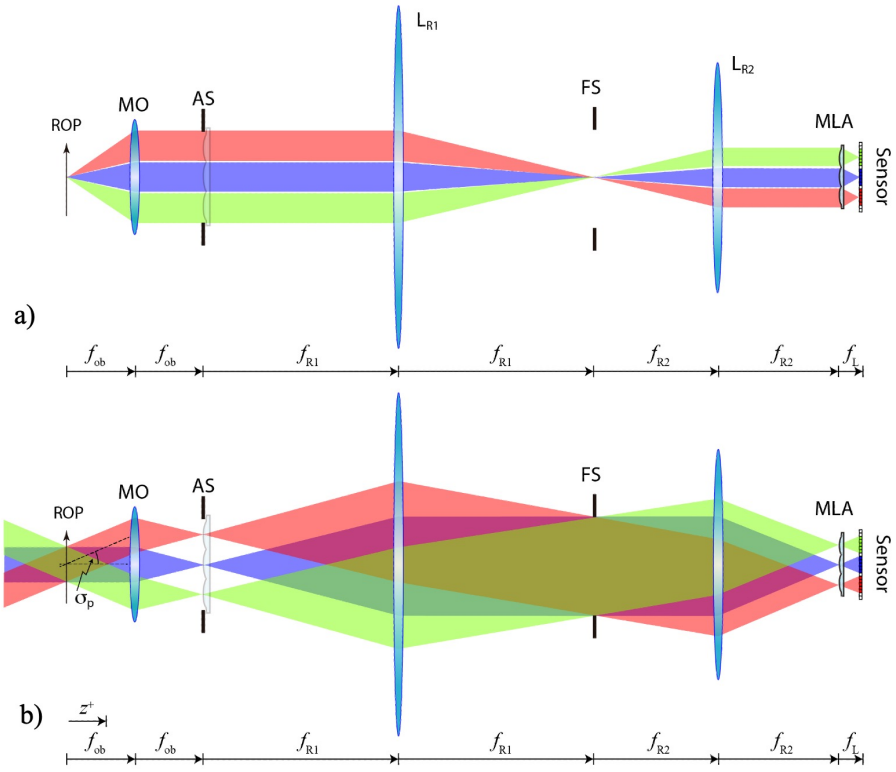

Fig. 1. Layout of the FLMic and ray tracing of light proceeding from the center of the ROP. (a) Aiming to make explicit the virtual insertion of the MLA at the AS, we have plotted a shaded MLA at the AS plane. (b) The lightbeams that pass through the optical centers of the microlenses are plotted. Axial coordinate, z, in the object space takes origin at the ROP.

In Fig. 1(b), it is illustrated the importance of the field stop and the orthographic nature of the EIs. The ROP, the field stop and the sensor are conjugated. The field stop plays the role of avoiding the overlapping between EIs. Then its diameter should fulfill the relation

$$\phi_{FS} = \frac{f_{R2}}{f_L} p \ . \tag{3}$$

Also interesting in the figure is the ray tracing in the object space. Since the ROP is set at the MO front FP, other parts of the sample are in front or behind that plane. The EIs of the ROP are identical, with no disparity. However, parts of the 3D sample in front of the ROP are captured with positive disparity, and parts behind with negative disparity. Interesting is that in the object space, the ray beams are collimated. This means that all the sections of the 3D sample are captured with the same magnification; in other words, all the EIs have an orthographic perspective. Any perspective is characterized by its parallax angle, which is an integer multiple of

$$\sigma_p = \frac{f_{R1}}{f_{R2} f_{ob}} p. \tag{4}$$

The higher the parallax angle, the better the captured 3D information.

Next, we revisit the basic equations that govern the FLMic image capture. First, the field of view (FOV) of captured EIs is

$$FOV_{EI} = \frac{1}{M_T} p. \tag{5}$$

where

$$M_T = \frac{f_L f_{R1}}{f_{ob} f_{R2}}. \tag{6}$$

is the lateral magnification between the ROP and the sensor.

The resolution limit of captured EIs is [34]

$$\rho_{EI} = max \left\{ \frac{\lambda}{2\mathrm{NA}_{\mathrm{ef}}} + \frac{\delta}{M_T} \, , \, \frac{2\delta}{M_T} \right\} \tag{7}$$

where δ is the sensor pixel size. Note that ρ_{EI} is the minimum distance between resolvable points and is usually expressed in microns. However, since the resolution capability of optical systems is usually evaluated in terms of the USAF resolution chart, it is common to use the inverse of ρ_{EI}, which is usually expressed in line pairs per millimeter (lp/mm).

Finally, the depth of field of captured EIs is given by [23]

$$DoF_{EI} = \frac{\lambda}{\mathrm{NA}_{\mathrm{ef}}^2} + \frac{\delta}{\mathrm{NA}_{\mathrm{ef}} \, M_T}. \tag{8}$$

3. Depth Reconstruction

The use of FLMic aims to achieve any, or all, of the three following purposes. The first is using, directly, the captured EIs for composing a movie in which the sample is watched from different perspective angles. The second is the calculation of refocused images at different depths. Third is the computation of 3D point clouds. These there purposes are closely linked. For example, from accurate point clouds, it is possible to generate new perspective views, which than can be watched free of occlusions [35]. Behind these algorithms, there is a protocol that is based on shifting the EIs and compound their pixels. The primary refocusing algorithm, the one named as the shift and sum (S & S) algorithm, is the result of shifting and summing the pixels of the EIs [36]. This process is illustrated in Fig. 2. When all the EIs are stacked with no relative shifting between them ($n_s = 0$) and the pixel values are summed, the irradiance distribution at the ROP is rendered. In the general case, any EI is shifted out a number of pixels n_s with respect to its neighbor. There is a linear relation between the number of pixels of the relative shifting, n_S, and the depth position, z_R, of the refocused plane. The relation is

$$z_R = \frac{n_s \delta_{\mathrm{rop}}}{\sigma_p}, \tag{9}$$

with $-N < n_s < N$, being N the number of pixels contained, along a Cartesian direction, by any EI. Here δ_{rop} is the sensor pixel size as back-projected onto the ROP, $\delta_{\mathrm{rop}} = \delta / M_T$ (δ being the actual pixel size) and $\delta = p/N$. As shown in Fig. 1(b), z_R takes its origin at the ROP and is positive for planes towards the MO.

A denser depth sampling can be obtained by simply resizing the EIs by an integer factor n, so that now the EIs have $N' = n.N$ pixels. This artificially makes the pixels smaller by a factor n, $\delta' = \delta/n$, and therefore makes the depth refocusing denser in depth by the same factor. The main drawback of this is the increment in computation time [37].

Finally, to avoid obtaining refocused images with different sizes, all the computed images are cropped at the ROP image size (shown in yellow in Fig. 2). This is possible provided that the region of interest of the sample is just in front of the central EI.

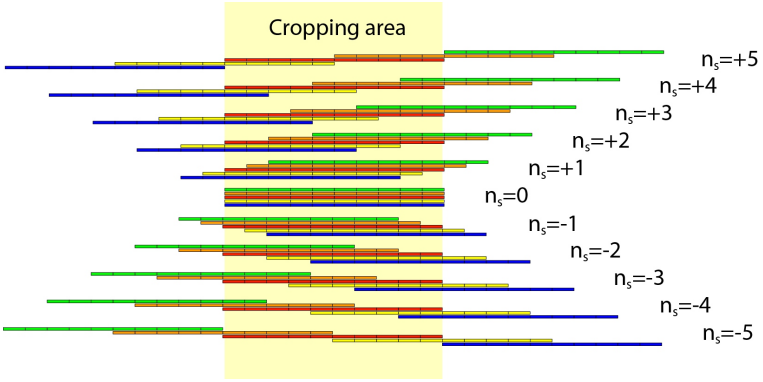

Fig. 2. Scheme of the shift & sum algorithm. Here we have represented a number of EIs (5 in this case) with a different colour each.

4. Setting up the FLMic

Aiming to build a FLMic in the laboratory, first one has to select its optical components according to the resolution, DoF, and FOV requirements. Also one should adapt to her/his stock of elements and to off-the-shelf ones. In our case, for example, the limiting element is the MLA, since we have only a few. For this experiment, we selected one with pitch $p = 1.0\ mm$ and focal length $f_L = 6.43\ mm$ (manufactured by Advanced Microoptic Systems GmbH). Making use of the software provided in [33], we selected the other elements: (a) An MO with magnification $M_{ob} = 20\times$ ($f_{ob} = 9.0\ mm$) and NA = 0.40; (b) A relay system composed by lenses of focal lengths $f_{R1} = 100\ mm$ and $f_{R2} = 50\ mm$; (c) An iris diaphragm with diameter $\phi_{FS} = 7.8\ mm$; and (d) A colour CMOS with pixel size $\delta = 2.2\ \mu m$. With these elements, it is expected to capture EIs with $\rho_{EI} = 4.24\ \mu m$, $DoF = 62.5\ \mu m$, and $FOV = 699.8\ \mu m$.

Then, one must follow the next steps, which are summarized in the video Visualization 1. The lenses used must be set according to the optical conjugation requirements and NA matching. In this practical guide, the image of the shear plate and the images of light pointers being imaged by the image sensor are a confirmation procedure to find the optimal position of elements precisely and efficiently.

4.1. Setting up the collimated beam

First, we need to implement a collimated light, which is used for the alignment and adjustment of forthcoming elements. We use a converging lens that collects the light proceeding from a fiber coupled to a laser, or by an LED. Such a collimating lens (with focal length $f_C = 50\ mm$ in our case) provides the plane wave. It is checked with the help of a shear plate (see Fig. 3).

4.2. Setting up the MLA and the image sensor

Next, the MLA and the sensor should be set parallel to each other and perpendicular to the optical axis. To fix the distance between the MLA and the sensor accurately, the sensor position is tuned so that an array of light points is captured. This ensures that the sensor is at the MLA back FP (see Fig. 4).

4.3. Setting up the telecentric relay system

The telecentric relay is composed of three elements; lens $R2$, iris diaphragm, and lens $R1$, which should be set sequentially. The first element to set is lens $R2$. As shown in Fig. 5, the lens is set in the optical bench perpendicular to the parallel beam and centered in height. To make sure

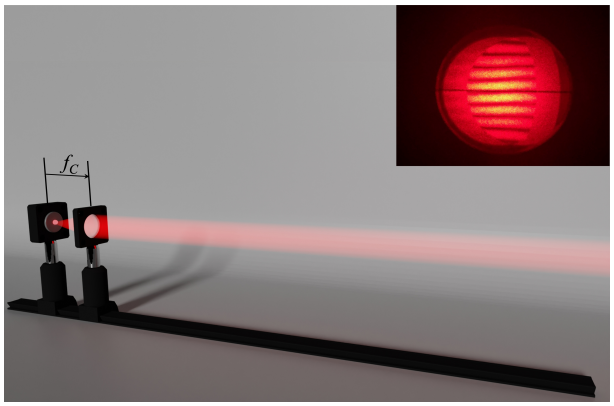

Fig. 3. Setting up the collimated beam.

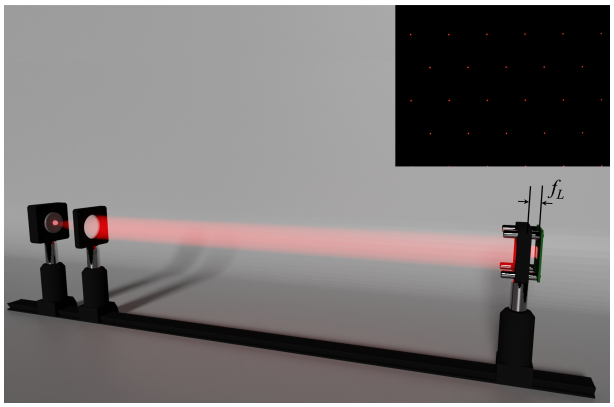

Fig. 4. Setting the MLA and the image sensor.

that the MLA is at the $R2$ back FP, the axial position of $R2$ is tuned till only one microlens is illuminated, which happens when the sensor records sharply a single hexagon.

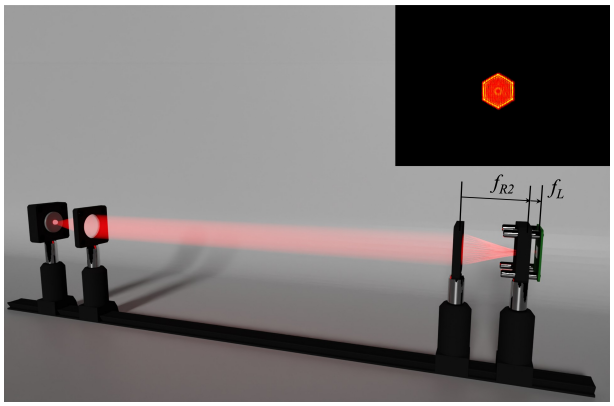

Fig. 5. Setting the lens $R2$.

The iris diaphragm, acting as a field stop, is an important element in the system since it helps

to avoid the overlapping between elemental images. It must be placed, properly centered, at the front FP of $R2$. In that case, the iris and the sensor are on conjugate planes. To make this, the iris is closed to a small diameter, and axially tuned till a sharp tiny circle is recorded (see Fig. 6).

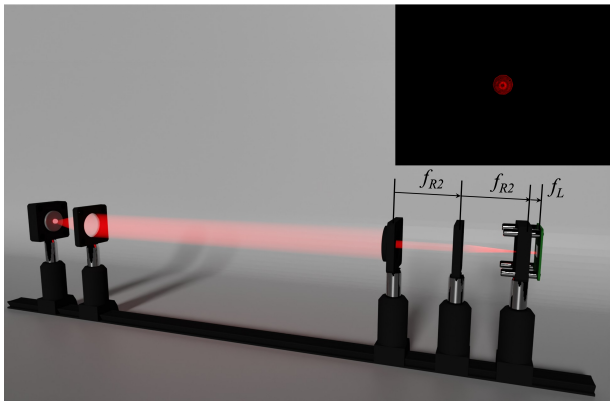

Fig. 6. Setting the iris.

Lens $R1$ must conform a telecentric relay together with $R2$. To ensure this, lens $R1$ should be placed, properly centered, in the optical bench, and its axial position tuned till the array of light spots is captured again by the sensor (see Fig. 7).

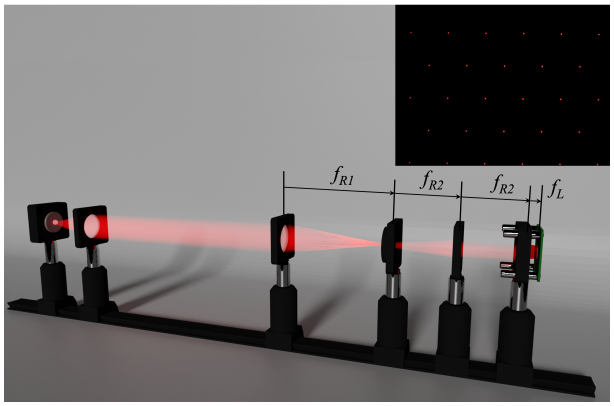

Fig. 7. Setting lens $R1$.

4.4. Setting up the microscope objective

The MO should be set telecentrically with lens $R1$. To ensure this, the MO should be placed, properly centered, in the optical bench, and its axial position tuned till only one microlens is illuminated, which happens again when the sensor records sharply a single hexagon (see Fig. 8).

4.5. Obtaining elemental images from the built FLMic.

Now one can record EIs after placing the sample on the front FP of the MO as shown in Figure 9. Similarly, it is possible to freely install the necessary light source in the illumination part according to the sample requirement.

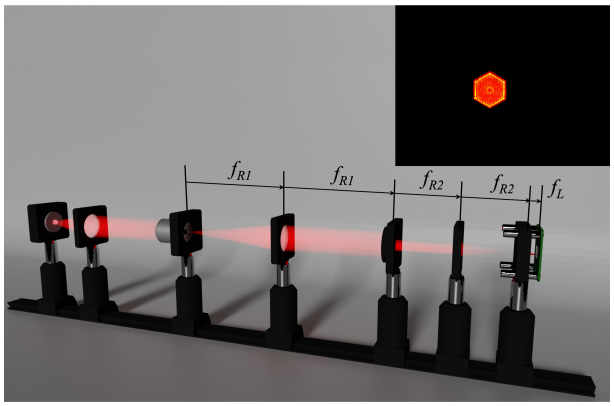

Fig. 8. Setting the MO.

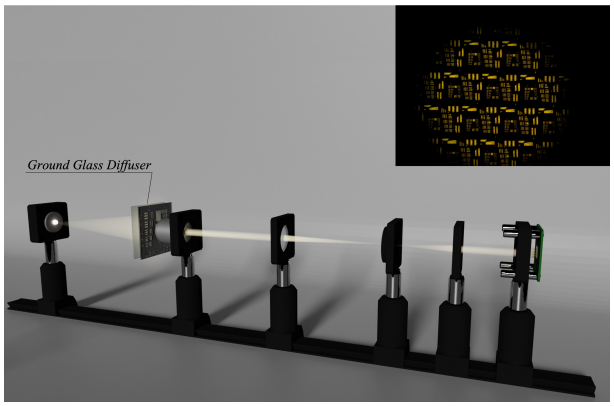

Fig. 9. Capturing the elemental images.

5. FLMic Performance Results

In order to verify the setup, one can evaluate the optical performance of the FLMic by using the system built following the previous section. According to the above formulae, the number of the EIs captured, along the horizontal direction, by our setup is $N_{EI} = 3.6$. Each EI has a circular shape with a diameter of 455 pixels.

5.1. The spatial resolution of FLMic

To confirm the spatial resolution of FLMic, we imaged the USAF 1951 target. Fig. 10(a) shows the captured raw images and it is also shown the central EI detailed in Fig. 10(b). The area visible in the selected image in Fig. 10(b) corresponds to Group 7 in the USAF target. Fig. 10 (c) shows the normalized profile of Group 7. It is possible to identify targets up to element 5 (E5), and through this, the highest spatial frequency of the USAF test calculated is 203 lp/mm ($\rho_{EI} = 4.9\ \mu m$). From Eq. (7) the expected value of resolution is $\rho_{EI} = 4.24\ \mu m$. In Visualization 2 a video shows, sequentially, the captured EIs. From this video, it is apparent that each EI has captured a slightly different region of the USAF chart. This is because indeed the chart was not set exactly at the ROP but at some distance from it. Probably this is the reason for not having reached the expected resolution limit.

To confirm this, we applied the S & S algorithm and found that the USAF chart was reconstructed sharply only for a shift $n_S = -9$, corresponding to $z_R = -62.4\ \mu m$. Fig. 11 shows the result of

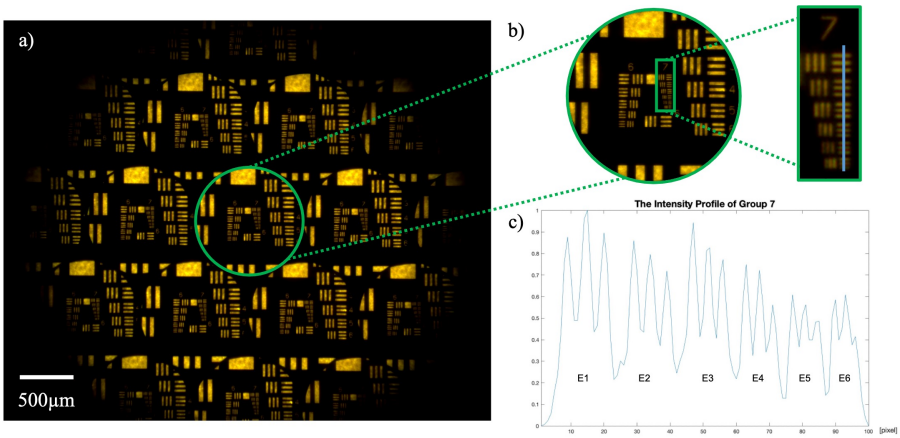

Fig. 10. The spatial resolution of Elemental images from FLMic system. (a) The captured raw elemental image of the USAF 1951 target (b) The central EI from raw image (c) The normalized profile along the blue line crossing Group 7.

the refocused image. Likewise, when checking Group 7 of the reconstructed image, it can be seen that the contrast is slightly reduced by the operation, but it still has the same spatial resolution as the captured EIs.

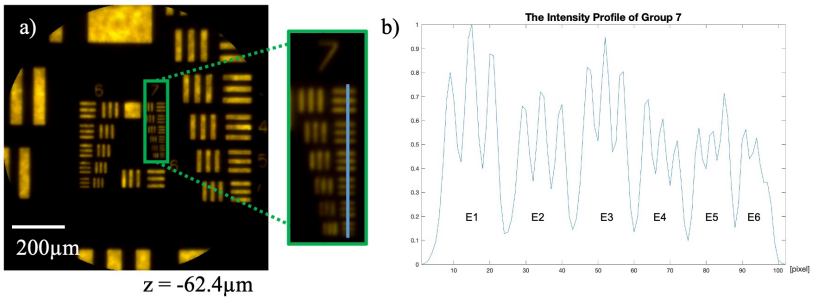

Fig. 11. The reconstruction result by using EIs of USAF 1951 test at the refocused plane $z_R = -62.4\ \mu m$.

5.2. The depth Reconstruction of FLMic

To confirm the range of reconstructed depths in the same setup, we used a 3D bio-sample, which is a leg of a grasshopper. Fig. 12 (a) shows the captured EIs. Additionally, in Visualization 3 a video shows, sequentially, the captured EIs. Again we used the S & S algorithm to reconstruct a 3D image. Specifically, reconstructed images correspond to 10 refocused planes with a spacing of 6.9 μm, see Fig. 12 (b). It can be seen that the DoF ranges from $z = -55.4\ \mu m$ to $z = +6.9\ \mu m$ (62.3 μm in total). In Visualization 4 a video shows the computed depth images sequentially.

5.3. FLMic application with fluorescence sample

Next, as a second example, we used the FLMic to handle a fluorescent sample. Aiming to obtain more perspective images we have changed the MO (now $M_{ob} = 20\times$, $f_{ob} = 10.0\ mm$ and NA = 0.50) and the lenses of the relay so that $f_{R1} = 200\ mm$, $f_{R2} = 100\ mm$. With this

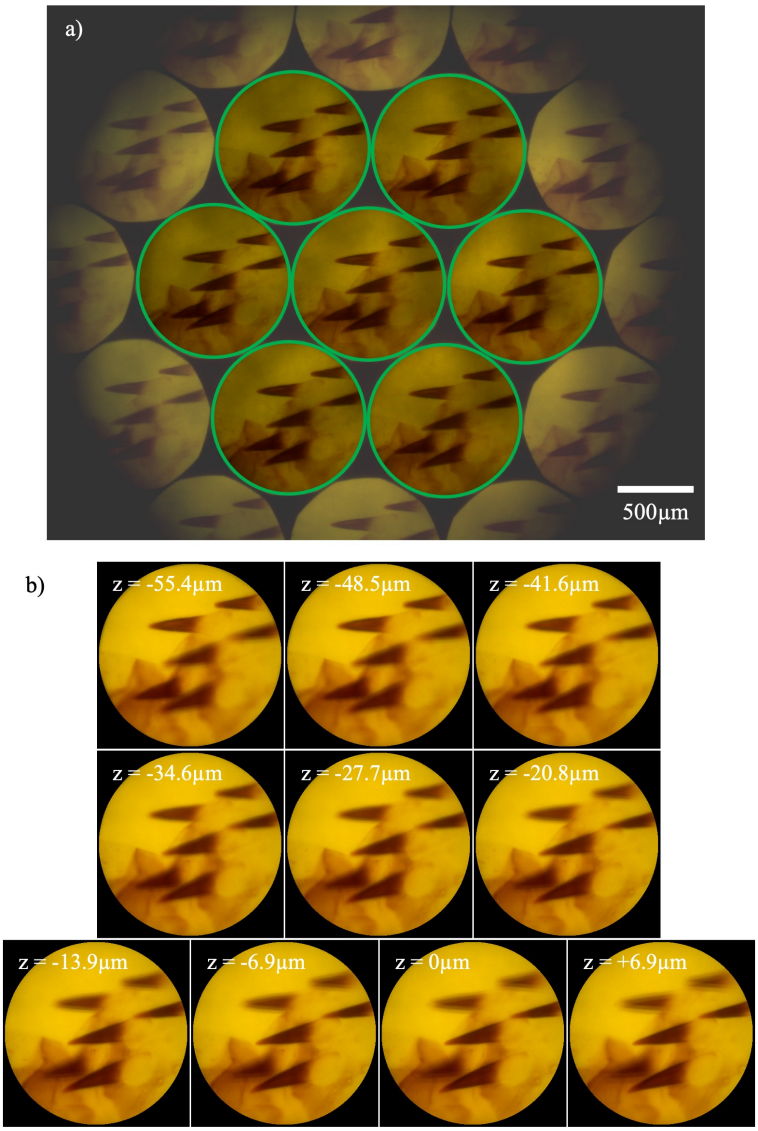

Fig. 12. (a)The captured raw elemental image of the 3D sample, leg of a grasshopper. (b) The reconstructed depth images.

new configuration, the expected figures about EIs are $N_{EI} = 5$, $\rho_{EI} = 4.7\ \mu m$, $DoF = 77\ \mu m$, and $FOV = 0.78\ mm$. Again the EIs have a circular shape with a diameter of 455 pixels. In Fig. 13(a) we show the captured EIs, where the ones that we use for the depth reconstruction are enhanced. Also, in Visualization 5 a video shows, sequentially, the captured EIs. This video makes apparent the high parallax achieved with the FLMic.

To calculate the depth refocused images, we used the (S & M) algorithm [18]. This algorithm is quite similar to the (S & S) one, but multiplying, instead of summing, the pixels of shifted EIs. When working with sparse fluorescent samples this algorithm is highly recommendable. The results obtained with this algorithm are shown in Fig. 13(b), where 11 depth images are shown. Finally, in Visualization 6 a video shows the computed depth images sequentially. The depth images are reconstructed from $z = -68.4\ \mu m$ to $z = +17.1\ \mu m$ and those are a total of 11 planes

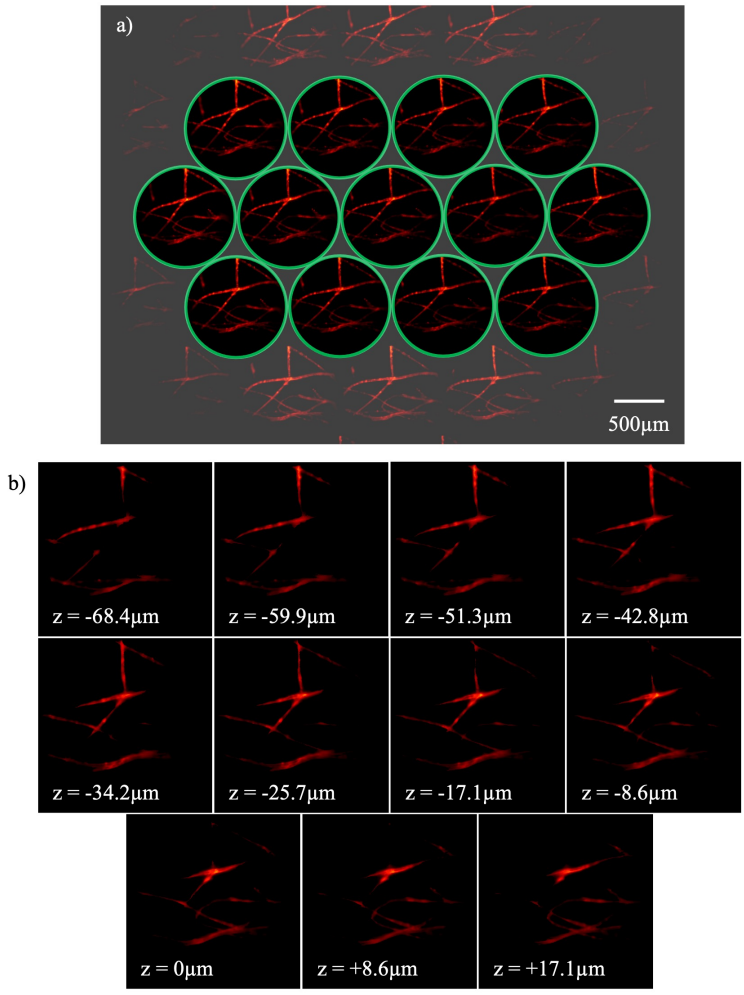

Fig. 13. FLMic with 3D fluorescence cotton fiber sample (a)The captured raw elemental image. (b)The reconstructed depth images.

constructed according to the spacing $8.6\mu m$.

6. Conclusion

This practical guide has provided a comprehensive overview of setting up the FLMic. We have covered FLMic's key concepts and techniques, including the optical feature of FLMic and the implementation process to meet the requirements. By following the step-by-step instructions provided in this guide, the reader will now have a solid understanding of how to face the accurate implementation of FLMic. Therefore, we hope that it has helped readers apply their newfound knowledge to their own work.

Funding. This research was funded by Grant PID2022-137747OB-I00, which is co-founded by the Ministerio de Ciencia, Innovacion y Universidades (Spain) and by the European Regional Development Fund. We acknowledge Generalitat Valenciana (Spain) under Grant CIPROM/2022/30.

Disclosures. The authors declare no conflicts of interest.

Data Availability Statement. The data presented in this study are contained within the article.

References

1. M. Martinez-Corral, P.-Y. Hsieh, A. Doblas, E. Sanchez-Ortiga, G. Saavedra, and Y.-P. Huang, "Fast axial-scanning widefield microscopy with constant magnification and resolution," J. Disp. Technol. **11**, 913–920 (2015).
2. M. Levoy, R. Ng, A. Adams, M. Footer, and M. Horowitz, "Light field microscopy," ACM Transactions on Graph. **25**, 924–934 (2006).
3. M. Levoy, Z. Zhang, and I. McDowall, "Recording and controlling the 4d light field in a microscope using microlens arrays," J. Microsc. **235**, 144–162 (2009).
4. M. Broxton, L. Grosenick, S. Yang, N. Cohen, A. Andalman, K. Deisseroth, and M. Levoy, "Wave optics theory and 3-d deconvolution for the light field microscope," Opt. Express **21**, 25418 (2013).
5. A. Llavador, G. Scrofani, G. Saavedra, and M. Martinez-Corral, "Large depth-of-field integral microscopy by use of a liquid lens," Sensors **18**, 3383 (2018).
6. N. Wagner, N. Norlin, J. Gierten, G. de Medeiros, B. Balázs, J. Wittbrodt, L. Hufnagel, and R. Prevedel, "Instantaneous isotropic volumetric imaging of fast biological processes," Nat. Methods **16**, 497–500 (2019).
7. Y. Zhang, Z. Lu, J. Wu, X. Lin, D. Jiang, Y. Cai, J. Xie, Y. Wang, T. Zhu, X. Ji, and Q. Dai, "Computational optical sectioning with an incoherent multiscale scattering model for light-field microscopy," Nat. Commun. **12** (2021).
8. G. Lippmann, "Epreuves reversibles donnant la sensation du relief," J. Phys. Theor. Appl. **7**, 821–825 (1908).
9. R. Prevedel, Y.-G. Yoon, M. Hoffmann, N. Pak, G. Wetzstein, S. Kato, T. Schrödel, R. Raskar, M. Zimmer, E. S. Boyden *et al.*, "Simultaneous whole-animal 3d imaging of neuronal activity using light-field microscopy," Nat. methods **11**, 727–730 (2014).
10. Y. Da Sie, C.-Y. Lin, and S.-J. Chen, "3d surface morphology imaging of opaque microstructures via light-field microscopy," Sci. reports **8**, 1–13 (2018).
11. P. Quicke, C. L. Howe, P. Song, H. V. Jadan, C. Song, T. Knöpfel, M. Neil, P. L. Dragotti, S. R. Schultz, and A. J. Foust, "Subcellular resolution three-dimensional light-field imaging with genetically encoded voltage indicators," Neurophotonics **7**, 035006 (2020).
12. J. Wu, Z. Lu, D. Jiang, Y. Guo, H. Qiao, Y. Zhang, T. Zhu, Y. Cai, X. Zhang, K. Zhanghao *et al.*, "Iterative tomography with digital adaptive optics permits hour-long intravital observation of 3d subcellular dynamics at millisecond scale," Cell **184**, 3318–3332 (2021).
13. A. Stefanoiu, J. Page, P. Symvoulidis, G. G. Westmeyer, and T. Lasser, "Artifact-free deconvolution in light field microscopy," Opt. express **27**, 31644–31666 (2019).
14. Y. Zhang, Z. Lu, J. Wu, X. Lin, D. Jiang, Y. Cai, J. Xie, Y. Wang, T. Zhu, X. Ji *et al.*, "Computational optical sectioning with an incoherent multiscale scattering model for light-field microscopy," Nat. communications **12**, 1–11 (2021).
15. A. Llavador, J. Sola-Pikabea, G. Saavedra, B. Javidi, and M. Martínez-Corral, "Resolution improvements in integral microscopy with fourier plane recording," Opt. Express **24**, 20792–20798 (2016).
16. G. Scrofani, J. Sola-Pikabea, A. Llavador, E. Sanchez-Ortiga, J. C. Barreiro, G. Saavedra, J. Garcia-Sucerquia, and M. Martínez-Corral, "Fimic: design for ultimate 3d-integral microscopy of in-vivo biological samples," Biomed. Opt. Express **9**, 335–346 (2018).
17. C. Guo, W. Liu, X. Hua, H. Li, and S. Jia, "Fourier light-field microscopy," Opt. Express **27**, 25573–25594 (2019).
18. E. Sánchez-Ortiga, G. Scrofani, G. Saavedra, and M. Martinez-Corral, "Optical sectioning microscopy through single-shot lightfield protocol," IEEE Access **8**, 14944–14952 (2020).
19. F. L. Liu, G. Kuo, N. Antipa, K. Yanny, and L. Waller, "Fourier DiffuserScope: single-shot 3d fourier light field microscopy with a diffuser," Opt. Express **28**, 28969 (2020).
20. N. Incardona, A. Tolosa, G. Scrofani, M. Martinez-Corral, and G. Saavedra, "The lightfield microscope eyepiece," Sensors **21**, 1457–1468 (2020).
21. G. Scrofani, G. Saavedra, M. Martínez-Corral, and E. Sánchez-Ortiga, "Three-dimensional real-time darkfield imaging through fourier lightfield microscopy," Opt. Express **28**, 30513–30519 (2020).
22. L. Cong, Z. Wang, Y. Chai, W. Hang, C. Shang, W. Yang, L. Bai, J. Du, K. Wang, and Q. Wen, "Rapid whole brain imaging of neural activity in freely behaving larval zebrafish (danio rerio)," Elife **6** (2017).
23. M. Martínez-Corral and B. Javidi, "Fundamentals of 3d imaging and displays: a tutorial on integral imaging, light-field, and plenoptic systems," Adv. Opt. Photonics **10**, 512–566 (2018).
24. Y.-G. Yoon, Z. Wang, N. Pak, D. Park, P. Dai, J. S. Kang, H.-J. Suk, P. Symvoulidis, B. Guner-Ataman, K. Wang *et al.*, "Sparse decomposition light-field microscopy for high speed imaging of neuronal activity," Optica **7**, 1457–1468 (2020).
25. B. Javidi, A. Carnicer, J. Arai, T. Fujii, H. Hua, H. Liao, M. Martínez-Corral, F. Pla, A. Stern, L. Waller *et al.*, "Roadmap on 3d integral imaging: sensing, processing, and display," Opt. Express **28**, 32266–32293 (2020).
26. R. R. Sims, S. A. Rehman, M. O. Lenz, S. I. Benaissa, E. Bruggeman, A. Clark, E. W. Sanders, A. Ponjavic, L. Muresan, S. F. Lee *et al.*, "Single molecule light field microscopy," Optica **7**, 1065–1072 (2020).
27. A. Stefanoiu, G. Scrofani, G. Saavedra, M. Martínez-Corral, and T. Lasser, "What about computational super-resolution in fluorescence fourier light field microscopy?" Opt. Express **28**, 16554–16568 (2020).
28. K. Yanny, N. Antipa, W. Liberti, S. Dehaeck, K. Monakhova, F. L. Liu, K. Shen, R. Ng, and L. Waller, "Miniscope3d: optimized single-shot miniature 3d fluorescence microscopy," Light. Sci. & Appl. **9**, 1–13 (2020).
29. Q. Cui, J. Park, Y. Ma, and L. Gao, "Snapshot hyperspectral light field tomography," Optica **8**, 1552–1558 (2021).
30. X. Hua, W. Liu, and S. Jia, "High-resolution fourier light-field microscopy for volumetric multi-color live-cell

imaging," Optica **8**, 614 (2021).
31. Z. Wang, L. Zhu, H. Zhang, G. Li, C. Yi, Y. Li, Y. Yang, Y. Ding, M. Zhen, S. Gao, T. K. Hsiai, and P. Fei, "Real-time volumetric reconstruction of biological dynamics with light-field microscopy and deep learning," Nat. Methods **18**, 551–556 (2021).
32. K. Kim, "Single-shot light-field microscopy: an emerging tool for 3d biomedical imaging," BioChip J. **16**, 397–408 (2022).
33. L. Galdón, G. Saavedra, J. Garcia-Sucerquia, M. Martínez-Corral, and E. Sánchez-Ortiga, "Fourier lightfield microscopy: a practical design guide," Appl. Opt. **61**, 2558 (2022).
34. L. Galdón, J. Garcia-Sucerquia, G. Saavedra, M. Martínez-Corral, and E. Sánchez-Ortiga, "Resolution limit in opto-digital systems revisited," Opt. Express **31**, 2000–2012 (2023).
35. J. Rostan, N. Incardona, E. Sanchez-Ortiga, M. Martinez-Corral, and P. Latorre-Carmona, "Machine learning-based view synthesis in fourier lightfield microscopy," Sensors **22**, 3487 (2022).
36. S.-H. Hong, J.-S. Jang, and B. Javidi, "Three-dimensional volumetric object reconstruction using computational integral imaging," Opt. Express **12**, 483–491 (2004).
37. B. Cho, P. Kopycki, M. Martinez-Corral, and M. Cho, "Computational volumetric reconstruction of integral imaging with improved depth resolution considering continuously non-uniform shifting pixels," Opt. Lasers Eng. **111**, 114–121 (2018).